J. Fluid Mech. (1981), *vol.* 108, *pp.* 1–18
Printed in Great Britain

Electrohydrodynamics in an electrostatic precipitator

By T. YAMAMOTO AND H. R. VELKOFF†
Corporate Research and Development, United McGill Corporation,
One Mission Park, P.O. Box 7, Groveport, Ohio 43125

(Received 10 April 1980)

Experimental and theoretical studies were undertaken to investigate the particulate-free secondary flow interaction in the wire-type electrostatic precipitator. The secondary flow generated by the corona discharge is not negligible, and strong flow interactions take place owing to the induced circulatory cells. The calculated numerical results demonstrate close agreement with experiment.

1. Introduction

Industrial electrostatic precipitators consist of a series of grounded parallel plates through which the dust-laden gas is passed. Equally spaced wire electrodes at high potential are located at the centre-line of the gas flow channel. Corona discharge at these electrodes causes ions to traverse the interelectrode space, and the great bulk of the particles acquire an electric charge of the same polarity as that of the discharge electrode. The charged particles move toward the collecting electrode under the influence of the electric field and are deposited. The particles captured on the collecting electrode are removed by rapping mechanisms and fall, under the influence of gravity, into hoppers. In the process of particulate collection in an electrostatic precipitator, the motion of particulates is affected by both electrostatic field and fluid forces. Among all existing theories, most of the efforts have been devoted to electrostatic action, but little attention has been given to the fluid dynamics coupled with the electrostatic field, i.e. electrohydrodynamics.

The fluid flow in a precipitator may be divided into the primary flow and secondary flow. The primary flow is the flow field that exists without the electrostatic field and is the gas flow through the precipitator. It is called cross-flow here. The secondary flow is the flow field caused by the corona discharge. The secondary flow is often called 'electric wind', 'corona wind' or 'ionic wind'. In the case of positive polarity, the positive ions which are created in the vicinity of the discharge electrode migrate toward the grounding electrode and give momentum to neutral molecules, thus providing a driving force to the fluid and causing the secondary flow. Since the ratio of the ions carried by the particles to the total ions is less than one per cent for most precipitator operations, the predominant current carrier is the ions. It is therefore assumed that the effect of the particles on the secondary flow is small.

The present study is based on the hypothesis that the influence of the secondary flow is not negligible. This is particularly true for collection involving submicron particles in which the migration velocity is small.

---

† Present address: Department of Mechanical Engineering, Ohio State University, 206 W. 18th Avenue, Columbus, Ohio 43210.

In the early studies no complete analytical solutions of the electric wind velocity were found. The main reasons were the unknown nature of the space-charge-density distribution and the boundary condition at the discharge wire due to the complicated nature of the corona discharge phenomena. The analytical solutions were limited to either zero space-charge density or constant charge density.

Ramadan & Soo (1969) presented analytical studies of the electric wind distribution in the absence of the cross-flow for the wire-plate geometry. The analytical solutions were limited to the model space-charge distribution.

Robinson (1976) has studied the electric wind distribution by using ion diffusion models and experimentally obtained helium-concentration profiles for the wire–plate geometry. Based on the results obtained, a circulatory motion was hypothesized for the wire–plate geometry.

Yabe, Mori & Hijikata (1978) have carried out a comprehensive analytical and experimental analysis of the electric wind for the single-wire plate in the open-channel geometry. The numerical solutions obtained showed a circulatory motion in the vicinity of the discharge wire.

This paper presents the experimental and computational studies on the particle-free secondary flow interactions using two-dimensional geometry. Two model configurations were considered: one-wire and two-wire arrangements in the flow channel. Measurements of current density, electrical potential distribution and pressure distribution were made. Flow interactions were visualized by a schlieren system and by using mist-injected smoke. Numerical studies include field- and space-charge calculations, and the calculations of secondary flow interactions. These results are compared with the experimental results. Based upon the results obtained, the effects of the secondary flow on the primary flow through an electrostatic precipitator may be very important.

2. Experimental study

A schematic diagram of the test arrangement is shown in figure 1. Air is drawn in through a large entrance where flow straightening is provided by a stacked array of soda straws. A contraction ratio of eight to one was used to provide a gas flow through the test section with low turbulence intensity and well-defined streamlines. Wire-to-plate spacing d is 3·0 cm and the distance between adjacent wires $2s$ is 4·8 cm for the two-wire arrangement. The first wire is 15·0 cm from the channel entrance. The total length of the flow channel is about 2·5 m. Flow rate is controlled by a damper in the exhaust duct and the flow velocity is measured by a hot-wire anemometer, calibrated by using a reference jet of known velocity. The corona discharge wires are 0·20 mm in diameter and 19·0 cm in length, with a high positive electrical potential.

(a) *Current density and pressure distribution*

Current density is measured for numerical calculation of the electric field and the space-charge distribution. To measure current density, 1·6 mm diameter brass grounding rods placed 6·4 mm apart are mounted on a Plexiglas plate. The rods are connected to a d.c. microammeter to obtain the corona current. Between the rods, a series of 1·6 mm diameter holes spaced every 6·4 mm are used for pressure measurements as shown in figure 2. Seventeen glass tubes are connected to the holes. Dif-

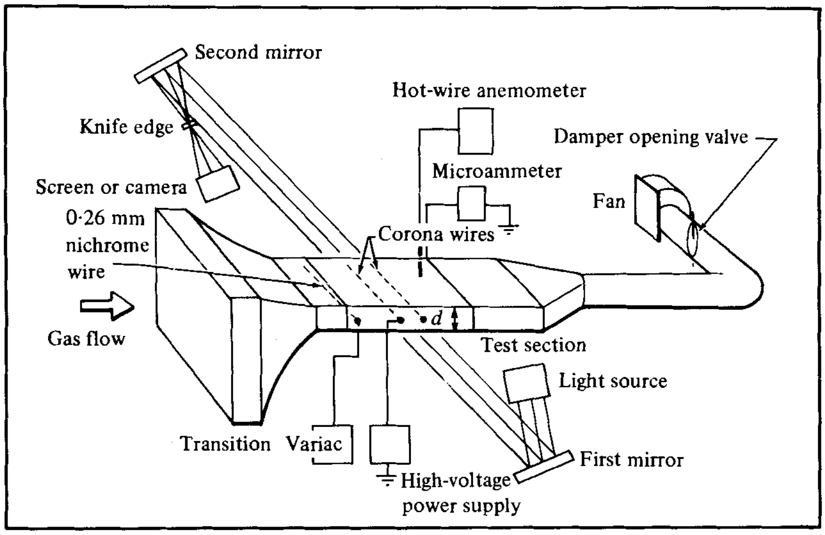

FIGURE 1. Schematic diagram of the test arrangement.

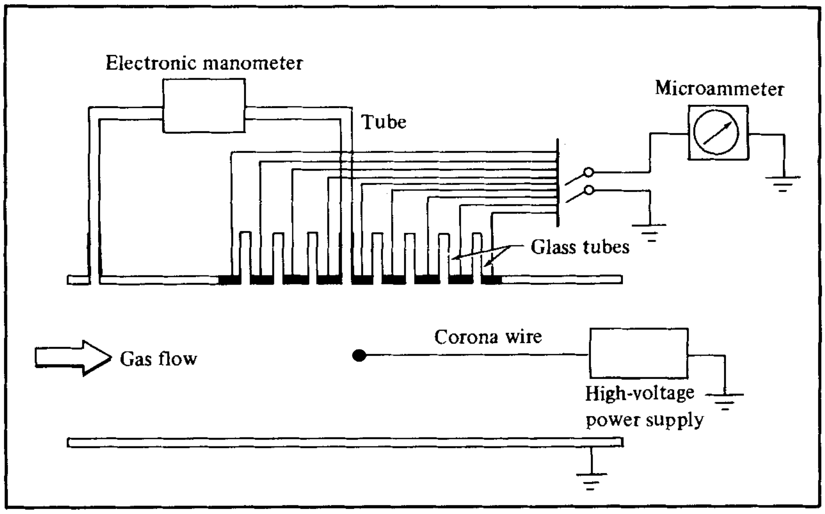

FIGURE 2. Schematic diagram for current and pressure measurement.

ferential pressures are measured using a high-precision electronic manometer with 1·0 per cent of full-scale accuracy. The rods were replaced by conductive silver-paint stripes, 1·6 mm wide with 3·2 mm intervals, when the cross-flow was introduced in order to avoid rod interference with the cross-flow.

For the measurement of the current density, each rod or conductive painted stripe is connected to one of two terminals. The current at any particular rod or stripe is read from the microammeter by connecting it to the meter terminal and connecting the other rods or stripes to the ground terminal as shown in figure 2. Current density distributions are obtained, for both no cross-flow and for various magnitudes of cross-flow.

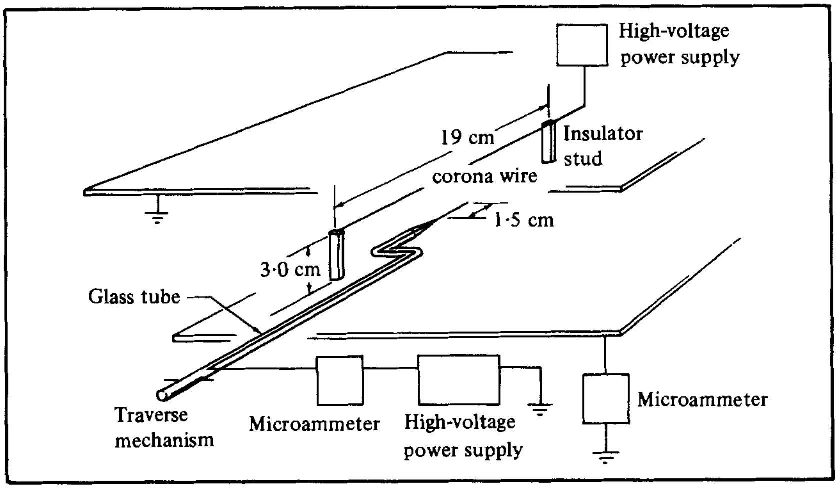

FIGURE 3. Electrical-potential measurement by an electrostatic Langmuir probe.

Local pressures are measured with respect to a reference pressure. The reference pressure is taken 9·0 cm upstream of the corona wire in a location chosen so that the pressure due to the corona discharge is negligible. Pressures are also measured with various cross-flow velocities.

(b) *Electrical potential measurement*

The experimental set-up for electrical potential measurements is shown in figure 3. An electrostatic Langmuir probe is used to measure local potential. The probe consists of a fine wire 0·09 mm in diameter and 1·5 cm in length. It is placed in parallel to the corona wire and covered with the tapered glass tube except for an exposed wire tip. A positive electrical potential is applied to the probe by a second power supply to cancel the current reading of a microammeter located in the probe circuit, as shown in figure 3.

The electrostatic probe is placed between the electrodes and traversed through the whole space except near the corona wire. The probe current is controlled by adjusting the probe potential. When the probe exceeds a certain potential, the probe current becomes zero, indicating there are no positive ions flowing to the probe. The surrounding potential is essentially balanced with the probe potential. As the probe potential is further increased, the probe itself starts to discharge to the surroundings and results in negative probe current. Therefore, the lowest potential for no probe current can be regarded as the space potential at that point. All experiments are carried out at room temperature and atmospheric pressure.

(c) *Flow visualization*

The schlieren optical technique is utilized to observe the possible flow interactions due to the presence of the corona discharge in the flow channel. Figure 1 shows the arrangement of the schlieren equipment. Light from a stroboscope is passed through a slit to provide a line source of light. The light is collimated by the first mirror, passed through the test section, brought to focus by a second mirror and then projected onto a screen. A knife edge is introduced at the focal point. The schlieren technique depends upon the

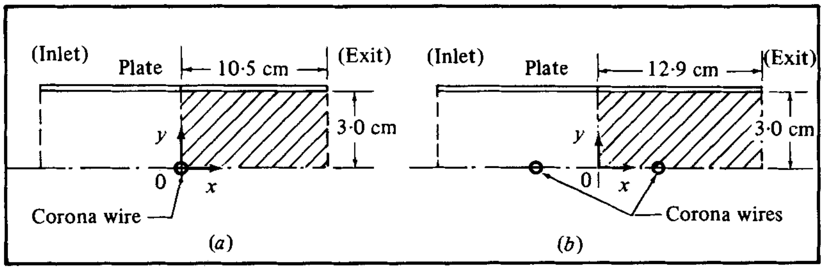

FIGURE 4. Model configuration for the wire–plate geometry. (*a*) One-wire configuration; (*b*) two-wire configuration.

presence of density gradients in the fluid being studied in order to indicate flow structure. To produce density gradients in the low-velocity stream used in these tests (0 to $1\cdot 8\,\mathrm{m\,s^{-1}}$), two heated wires are placed at 7 cm upstream from the corona wire. This location is sufficiently far from the corona wire to avoid interference with the high field near the corona wire. The wires are heated with a.c. power at this location, but in some cases when the heated wires are placed nearer the corona wire d.c. power is used. The d.c. battery and the heated wire are allowed to float electrically with respect to the ground.

By placing the heated wire at various cross-channel positions, it is possible to provide illumination of the stream at different locations away from the active corona wires. Photographs were taken of the schlieren patterns observed in the test section. Since the heated wake from the nichrome wires could possibly be influenced by buoyancy, specific tests were run to check this. It was found that no significant buoyant influences occurred as long as the flow velocity was above $8\,\mathrm{cm\,s^{-1}}$.

(*d*) *Motion of charged particles*

The gross movement of particles in the electrohydrodynamic field are observed by the introduction of mist particles in the cross-flow gas stream. Solid particulates cannot be used for this type of observation, because of particle re-entrainment that can take place under the influence of the secondary flow and the repulsive force, owing to induced and contact charging during particle residence on the plate. The mist was obtained with a smoke generator which used mineral oil and carbon dioxide. The smoke was admitted in front of the soda straws at the inlet of the transition section. The distribution of the mist was recorded by a ciné camera for various cross-flow velocities and electrical potentials.

3. Numerical study

(*a*) *Field and space-charge-density distribution*

Since the driving force of the secondary flow is provided by the positive ions and the electric field, the calculations of the space-charge density and the electrical-field distribution precede the flow calculations. Numerical solutions for the field strength in the presence of the space charge are obtained by applying the numerical methods of Leutert & Bohlen (1972). The computational domains for the flow configuration with one wire and two wires are shown as hatched areas in figure 4.

The governing equations for the electric potential and space-charge-density distributions are written as

$$\operatorname{div}\operatorname{grad} V = -\rho_c/\epsilon_0, \tag{1}$$

$$\rho_c^2 = \epsilon_0 \operatorname{grad}\rho_c \cdot \operatorname{grad} V. \tag{2}$$

The electric field strength E and electric current density J are related to the potential V by

$$\mathbf{E} = -\operatorname{grad} V, \tag{3}$$

$$\mathbf{J} = \rho_c(K\mathbf{E}+\mathbf{u}) \simeq \rho_c K\mathbf{E}. \tag{4}$$

Since the ion velocity is two orders of magnitude faster than the fluid velocity, $K\mathbf{E} \gg \mathbf{u}$, (4) can be decoupled from the fluid velocity. The boundary conditions for V in the computational domain shown in figure 4 are written as

$V = V_0$ measured electrical potential at the wire,
$V = 0$ along the cathode plate,
$\partial V/\partial n = 0$ along any symmetry lines. (5)

The boundary condition for V at the flow exit cannot be defined uniquely. The distance, however, of the right boundary from the wire can be made sufficiently large compared with the distance between the wire and the plate so that the symmetry boundary condition may be used as an exit condition.

The calculation starts by solving the space-charge-free ($\rho_c = 0$) form of (1). Since the space-charge-density distribution is not known initially, the space-charge density at the wire is assumed. The entire charge-density distribution is calculated from the current continuity equation (2). The Poisson equation (1) is then solved by using the space-charge-density distribution so obtained. The total current at the plate is then calculated and compared with the experimentally determined total current. If they are different, a new value of charge density at the wire is assumed until the calculated total current at the collection plate approaches that measured for the given wire voltage. The detailed calculation procedure was reported by Yamamoto (1979) and Yamamoto, Nakamura & Velkoff (1980).

(*b*) *Flow interaction*

The basic equations for the flow field are the Navier–Stokes equations expressed in terms of the vorticity–stream-function form. The vorticity transport equation and the elliptic Poisson equation derived from the definition of vorticity and stream function are written as

$$\frac{\partial\overline{\omega}}{\partial\bar{t}} = -\frac{\partial\overline{\Psi}}{\partial\bar{y}}\frac{\partial\overline{\omega}}{\partial\bar{x}} + \frac{\partial\overline{\Psi}}{\partial\bar{x}}\frac{\partial\overline{\omega}}{\partial\bar{y}} + \frac{1}{R_{\mathrm{EHD}}}\left(\frac{\partial^2\overline{\omega}}{\partial\bar{x}^2} + \frac{\partial^2\overline{\omega}}{\partial\bar{y}^2}\right) + \left(\frac{\partial\bar{\rho}_c}{\partial\bar{x}}\frac{\partial\overline{V}}{\partial\bar{y}} - \frac{\partial\bar{\rho}_c}{\partial\bar{y}}\frac{\partial\overline{V}}{\partial\bar{x}}\right), \tag{6}$$

$$\frac{\partial^2\overline{\Psi}}{\partial\bar{x}^2} + \frac{\partial^2\overline{\Psi}}{\partial\bar{y}^2} = \overline{\omega}, \tag{7}$$

where the EHD Reynolds number R_{EHD} is based on the channel half-width d, the kinematic viscosity ν, and the characteristic velocity U_e. All quantities are dimensionless with reference to d, U_e, V_0 and the change density at the wire ρ_{c0}:

$$\overline{\omega} = d\omega/U_e, \quad \overline{\Psi} = \Psi/U_e d, \quad \bar{t} = U_e t/d, \quad \bar{x} = x/d, \quad \bar{y} = y/d,$$

$$\bar{\rho}_c = \rho_c/\rho_{c0}, \quad \overline{V} = V/V_0, \quad E_{\mathrm{EHD}} = dU_e/\nu, \quad \text{and} \quad U_e = (\rho_{c0}V_0/\rho)^{\frac{1}{2}}.$$

The above equations were numerically solved on the computational domain shown in figure 4. The inlet flow boundary condition was set to a uniform flow based on the inlet configuration of the experimental equipment. In terms of the vorticity and stream function, the uniform velocity is specified by

$$\bar{\Psi}(0,\bar{y}) = \bar{U}_0\,\bar{y}, \quad \bar{\omega}(0,\bar{y}) = \frac{\partial \bar{u}}{\partial \bar{y}} = \frac{\partial^2 \bar{\Psi}}{\partial \bar{y}^2} = 0. \tag{8}$$

For the outlet, the boundary condition was imposed by

$$v = -\frac{\partial \bar{\Psi}}{\partial \bar{x}} = 0, \quad \frac{\partial \bar{\omega}}{\partial \bar{x}} = 0. \tag{9}$$

The outlet boundary condition, above, implies that the parallel flow is established without specifying the flow-velocity distribution. This less restrictive boundary condition allows a considerably shorter computational domain for comparable accuracy in the region of interest (Roache 1972). The non-slip condition was applied along the channel wall:

$$\bar{\Psi} = \bar{U}_0, \quad \bar{\omega} = \frac{\partial \bar{u}}{\partial \bar{y}} = \frac{\partial^2 \bar{\Psi}}{\partial \bar{y}^2}. \tag{10}$$

Along the centre-line of the channel, the symmetry boundary condition was given by

$$\bar{\Psi} = 0, \quad \bar{\omega} = 0. \tag{11}$$

Finite-difference approximations for (6) were derived and solved as an initial-value problem by using the standard explicit method. At each time step, (7) was solved by using the fast direct-solution method (FDS method) (Nakamura 1977), for which no iterative calculations are necessary, resulting in significant reduction of computational time. The upwind difference scheme for the convection terms in (6) was used because it was found to eliminate numerical instability which occurred with central differences. In all cases, the flow calculations started with an appropriate initial condition and time was advanced until a steady state was reached.

4. Results

(*a*) *Current density, potential and pressure distribution*

Figure 5 illustrates the normalized current-density distributions for the one-wire configuration. The calculated distributions and measured distributions are compared for various applied potentials. The calculated current-density distributions agree well with the experimental results.

When velocities of up to 9·1 m s^{-1} were introduced, the current-density distribution was not significantly altered. From this it can be concluded that the ion flow is not influenced by the primary flow in the precipitator. This substantiates the assumption that the fluid velocity can be decoupled from the electrostatic field in calculating current density, equation (4).

For the two-wire configuration, the peak of current distribution is located under each discharge wire and the magnitude rapidly falls near the symmetry line between the adjacent wires. The current distribution for two wires is such that the integrated total current for the portion of the curve affected by the adjacent wire is approximately 25 per cent less than the total current for the portion of the curve away from the wire.

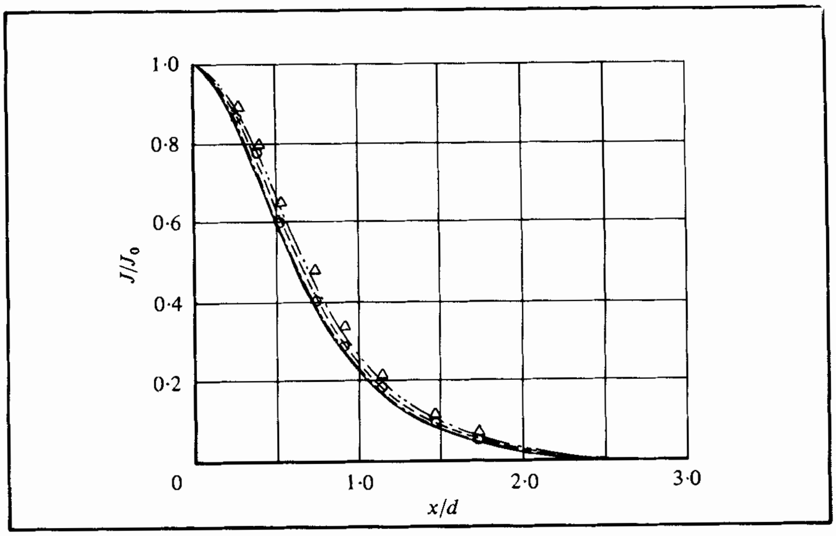

FIGURE 5. Normalized current-density distribution for the one-wire configuration. ——, $E_0 = 5{\cdot}83$ kV cm^{-1}, $I = 2{\cdot}47 \times 10^{-4}$ A; – · – · –, $E_0 = 5{\cdot}0$ kV cm^{-1}, $I = 1{\cdot}60 \times 10^{-4}$ A; – – –, $E_0 = 4{\cdot}17$ kV cm^{-1}, $I = 0{\cdot}876 \times 10^{-4}$ A; – ·· – ·· –, $E_0 = 3{\cdot}33$ kV cm^{-1}, $I = 0{\cdot}338 \times 10^{-4}$ A; ○, experimental results without cross-flow for $E_0 = 5{\cdot}0$ kV cm^{-1}; △, experimental results with $U_0 = 9{\cdot}1$ m s^{-1} for $E_0 = 5{\cdot}0$ kV cm^{-1}.

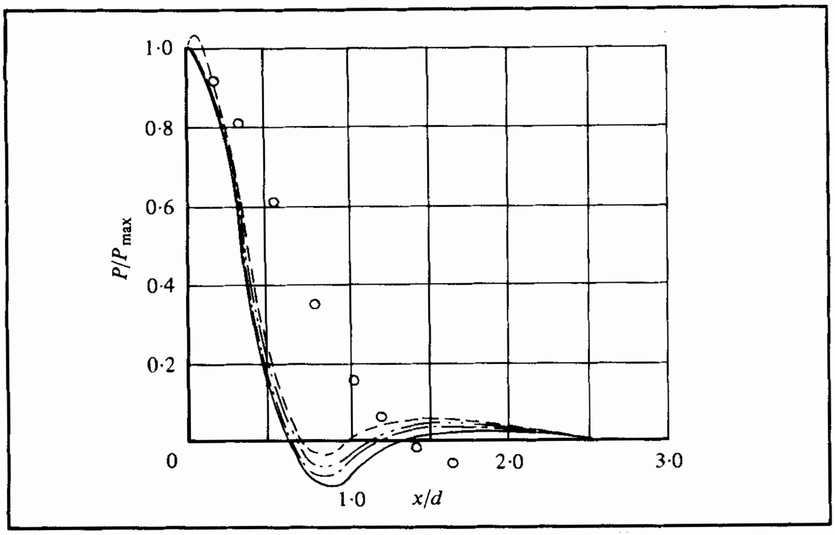

FIGURE 6. Normalized pressure distribution at the plate for the one-wire configuration. ——, $E_0 = 5{\cdot}83$ kV cm^{-1}; – · – · –, $E_0 = 5{\cdot}0$ kV cm^{-1}; – – –, $E_0 = 4{\cdot}17$ kV cm^{-1}; – ·· – ·· –, $E_0 = 3{\cdot}33$ kV cm^{-1}; ○, experimental results.

On the other hand, the pressure distributions are affected by the cross-flow velocities. The location of the pressure peak was found to shift downstream as a function of the cross-flow velocity. Maximum shift of the pressure peak reaches approximately 1·5 cm (i.e. 0·5d), and the pressure peak disappears when the primary flow exceeds 1·8 m s^{-1}, with an average field $E_0 = 5{\cdot}0$ kV cm^{-1}. Figure 6 illustrates the normalized pressure distribution at the plate for the one-wire configuration. It should be noted

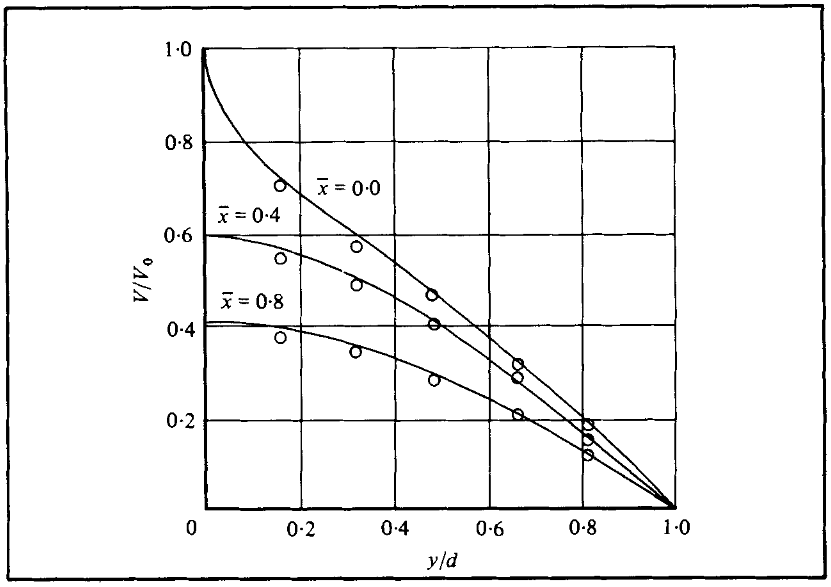

FIGURE 7. Comparison between experimental and theoretical potential distribution for the one-wire configuration. ——, theoretical results; ○, experimental results for $E_0 = 5·0\ \text{kV cm}^{-1}$, $I = 1·60 \times 10^{-4}$ A.

that the numerical pressure distribution is not equal to the experimental pressure distribution except at the stagnation point where the two pressures are normalized. A possible source of the difference lies in the difficulty of measuring the fluid velocity in a region of complex flow and high electrical fields. The pressure measured is the static pressure and may include a fraction of the velocity pressure as well. This may occur since the local velocity may not be perpendicular to the inlet of the particular pressure probe used.

Figure 7 illustrates the normalized potential distribution for the one-wire configuration. The calculated potential distribution compares well with the experimental results.

(*b*) *Flow interaction*

All the flow computations were performed for an electrical potential of 15·0 kV (i.e. average electric field of 5·0 kV cm^{-1}), while the primary flow velocity was varied from 0 to 1·8 m s^{-1}. The number of mesh points used for the one-wire configuration was 113 × 17 including boundaries, while that for the two-wire configuration was 139 × 17. It should be noted that the effects of the corona wire itself on the flow field are ignored because the wire radius is so small, relative to the channel size. The effect of the small wires would be largely confined to a region local to the wire, and with the corona discharge active this effect would be contained within the core of the electric wind jets formed. Besides, the linear statement of (1) is not applied in the corona glow region directly surrounding the corona wire.

The results of the present computations can be applied to estimate flow with other electrical potentials and channel widths if N_{EHD} and the atmospheric conditions are the same. N_{EHD} is the ratio of R_{EHD} to R. In other words, when non-dimensionalized, the flow distributions with different potential and channel width are similar if the N_{EHD} values are the same. It should be noted that the magnitude of the interactions

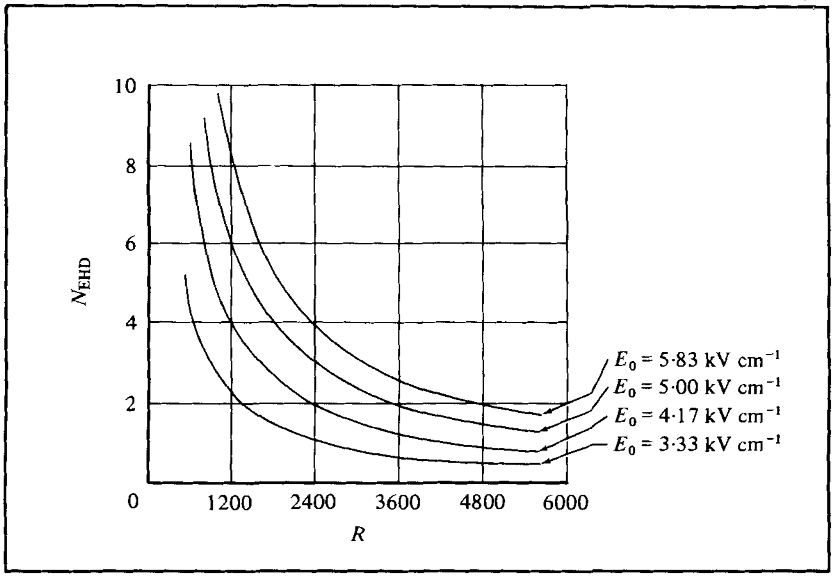

FIGURE 8. Interrelations between N_{EHD}, R and E_0.

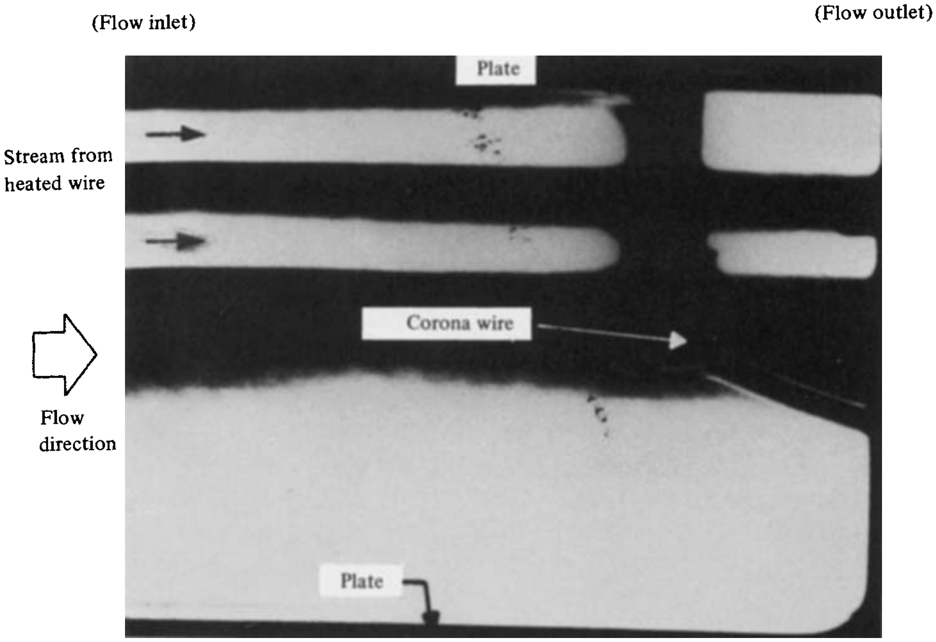

(a)

FIGURE 9(a). For legend see facing page.

between the primary and secondary flows is directly related to the magnitudes of the N_{EHD}. That is, the higher the N_{EHD} value, the more the contribution of the secondary flow. The interrelations between N_{EHD}, R and E_0 are illustrated in figure 8.

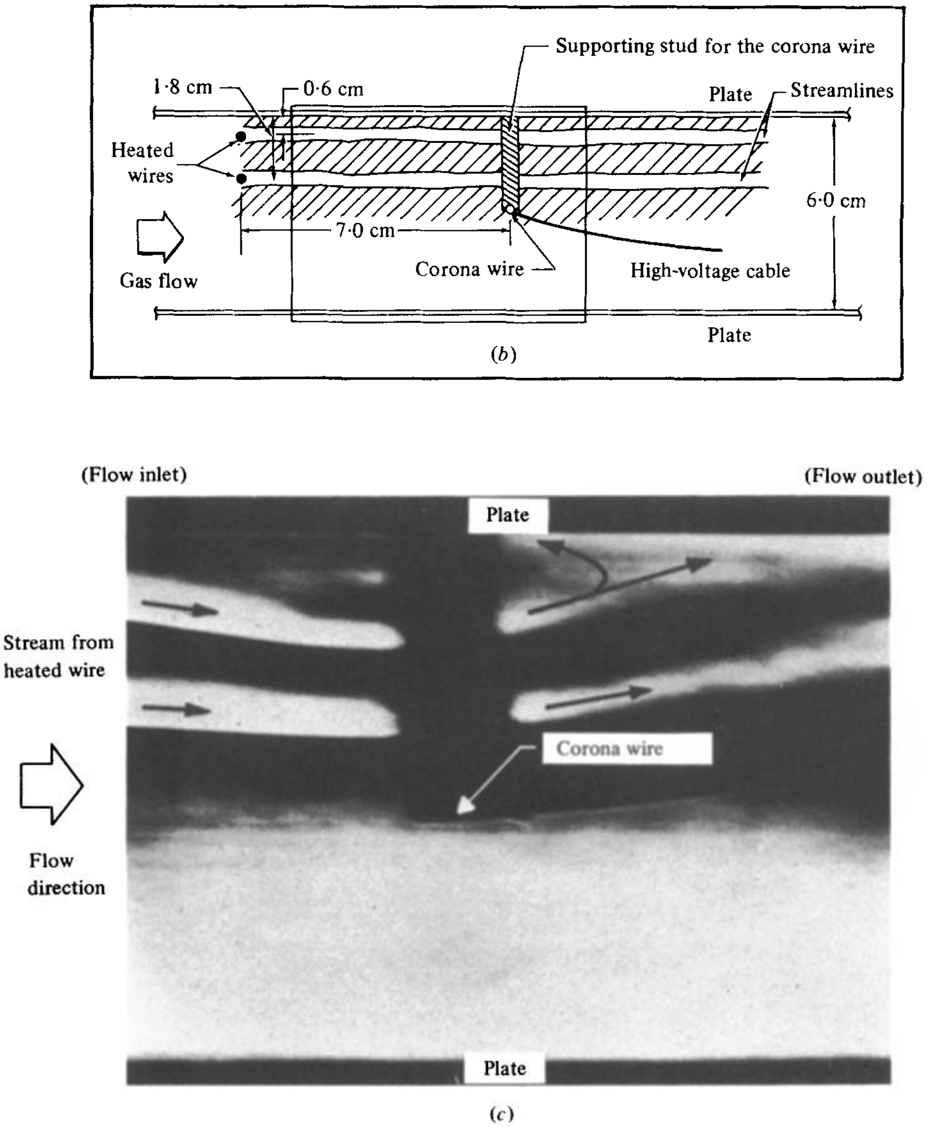

FIGURE 9. Experimental flow interaction for the one-wire configuration. (*a*) A streamline pattern in the absence of electric field, $U_0 = 0{\cdot}23$ m s^{-1}, $R = 900$. (*b*) A sketch of the streamline pattern of (*a*). (*c*) $U_0 = 0{\cdot}61$ m s^{-1}, $R = 2400$, $E_0 = 4{\cdot}17$ kV cm^{-1}.

One-wire configuration

Figures 9(*a*)–(*c*) illustrate the flow interaction between the secondary flow and the primary flow for various electrical potentials and cross-flow velocities for the one-wire configuration. Figures 9(*a*)–(*b*) show the case of cross-flow with no applied potential and figure 9(*c*) indicates the interaction for 4·17 kV cm^{-1}.

In interpreting these pictures, the flow direction is from left to right. The two heated wires are located upstream to the left of the picture. The air heated by the wires can be seen as two white strips, as shown in the picture. The lower portion of the figure provides an interpretation of the schlieren photograph. It shows that the dark vertical

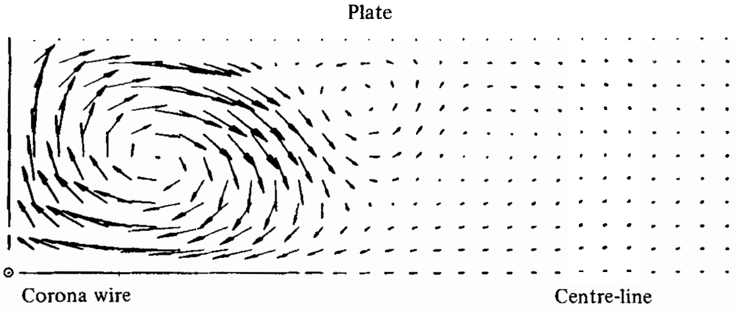

FIGURE 10. Computational electric wind velocity plot for the one-wire configuration. $E_0 = 5{\cdot}0 \text{ kV cm}^{-1}$, $R_{\text{EHD}} = 7499$, $u_{\max} = 1{\cdot}05 \text{ m s}^{-1}$, $\Delta x = 2\Delta y$.

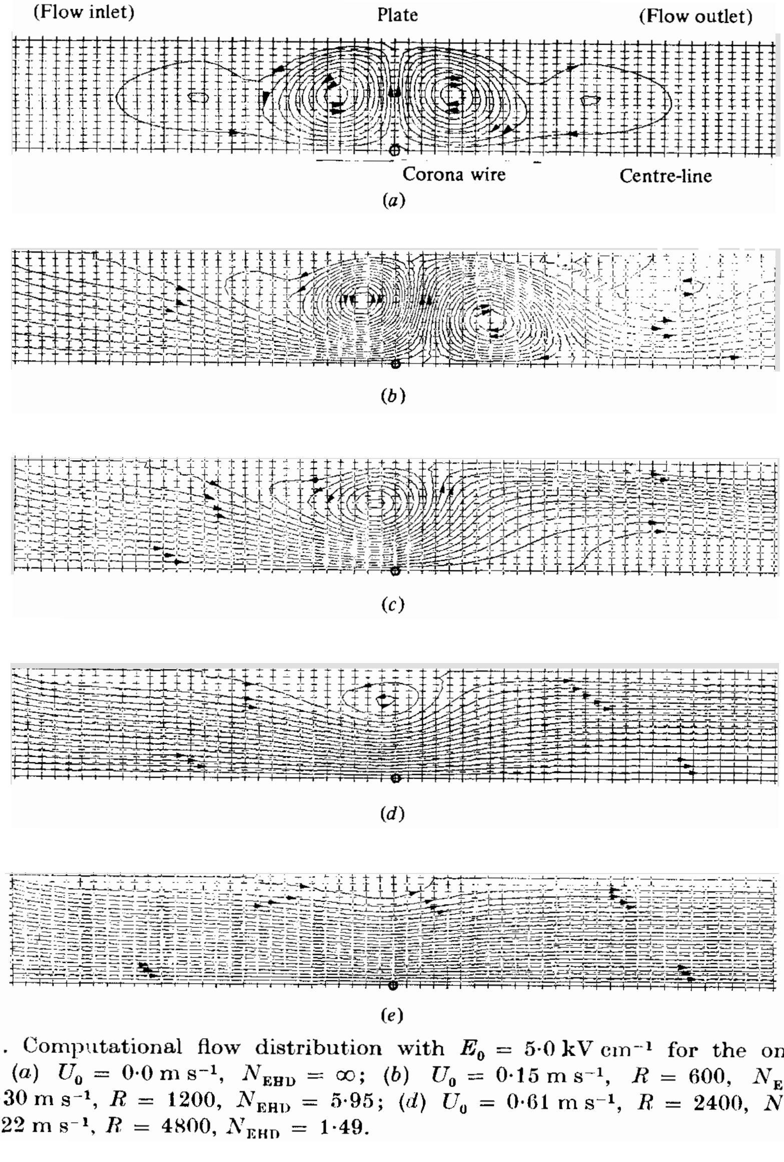

FIGURE 11. Computational flow distribution with $E_0 = 5{\cdot}0 \text{ kV cm}^{-1}$ for the one-wire configuration. (a) $U_0 = 0{\cdot}0 \text{ m s}^{-1}$, $N_{\text{EHD}} = \infty$; (b) $U_0 = 0{\cdot}15 \text{ m s}^{-1}$, $R = 600$, $N_{\text{EHD}} = 11{\cdot}90$; (c) $U_0 = 0{\cdot}30 \text{ m s}^{-1}$, $R = 1200$, $N_{\text{EHD}} = 5{\cdot}95$; (d) $U_0 = 0{\cdot}61 \text{ m s}^{-1}$, $R = 2400$, $N_{\text{EHD}} = 2{\cdot}98$; (e) $U_0 = 1{\cdot}22 \text{ m s}^{-1}$, $R = 4800$, $N_{\text{EHD}} = 1{\cdot}49$.

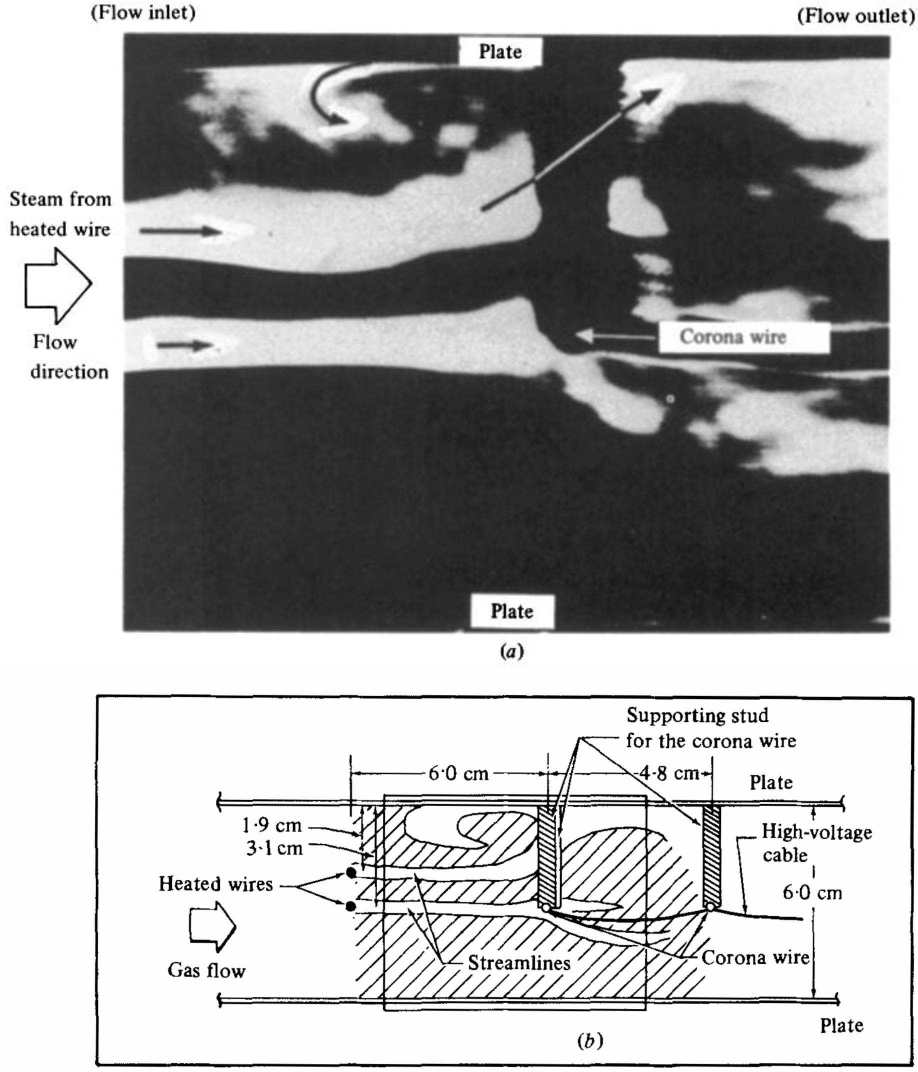

FIGURE 12 (*a*, *b*). For legend see next page.

region at the centre is due to blockage from the vertical posts that support the corona wire. The lower region of the pictures, below the corona wire, appear white, not because that area was heated, but rather because of the adjustment of the knife edge of the schlieren system. When good contrast was reached in the upper portion, often the lower portion would appear as a white band.

The computed velocities for the one-wire configuration with no cross-flow are shown in figure 10. These velocities are due solely to the electric wind.

Figures 11 (*a*)–(*e*) illustrate the case for the one-wire configuration at an applied voltage of 15·0 kV for various cross-flow velocities. The circulatory cells are clearly evident at low Reynolds number.

As the Reynolds number increases from zero, the pair of the major circulatory cells seen in the zero velocity case in figure 11 (*a*) are shifted downstream as illustrated in figure 11 (*b*). At $R = 1200$, figure 11 (*c*), one large counterclockwise cell is formed above

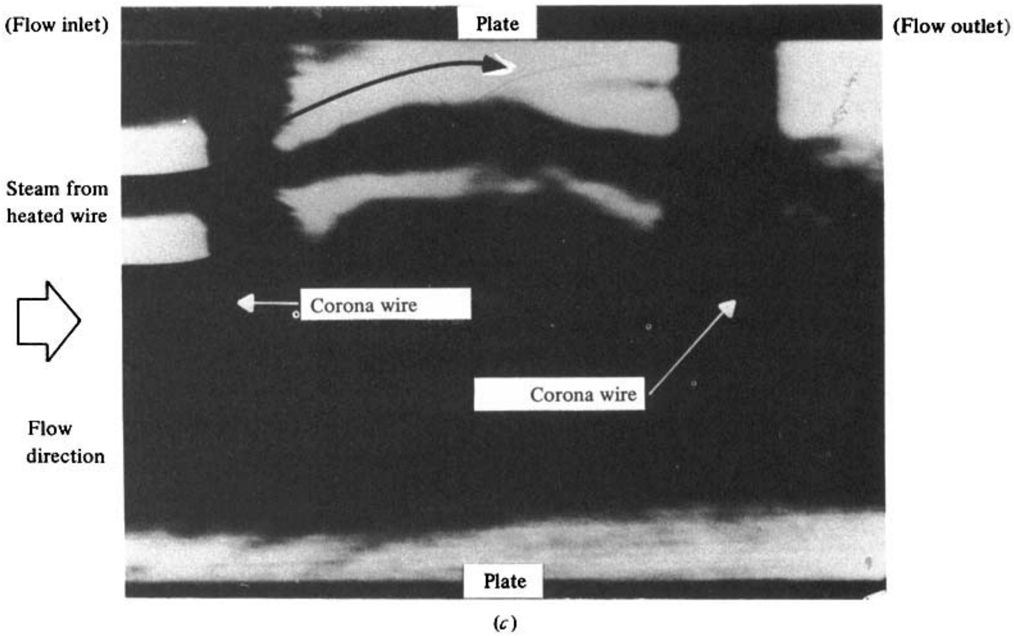

FIGURE 12. Experimental flow interaction for the two-wire configuration. (*a*) $U_0 = 0{\cdot}31$ m s^{-1}, $R = 1200$, $E_0 = 4{\cdot}17$ kV cm^{-1}; (*b*) a sketch of the streamline pattern of (*a*); (*c*) $U_0 = 0{\cdot}91$ m s^{-1}, $R = 3600$, $E_0 = 5{\cdot}0$ kV cm^{-1}.

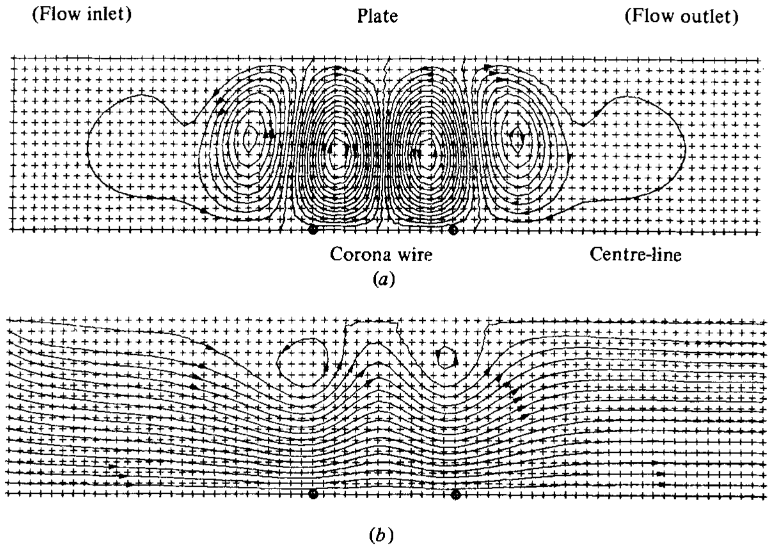

FIGURE 13. Computational flow distribution with $E_0 = 5{\cdot}0$ kV cm^{-1} for the two-wire configuration. (*a*) $U_0 = 0{\cdot}0$ m s^{-1}, $N_{EHD} = \infty$, $\Delta x = 2\Delta y$; (*b*) $U_0 = 0{\cdot}61$ m s^{-1}, $R = 2400$, $N_{EHD} = 2{\cdot}69$.

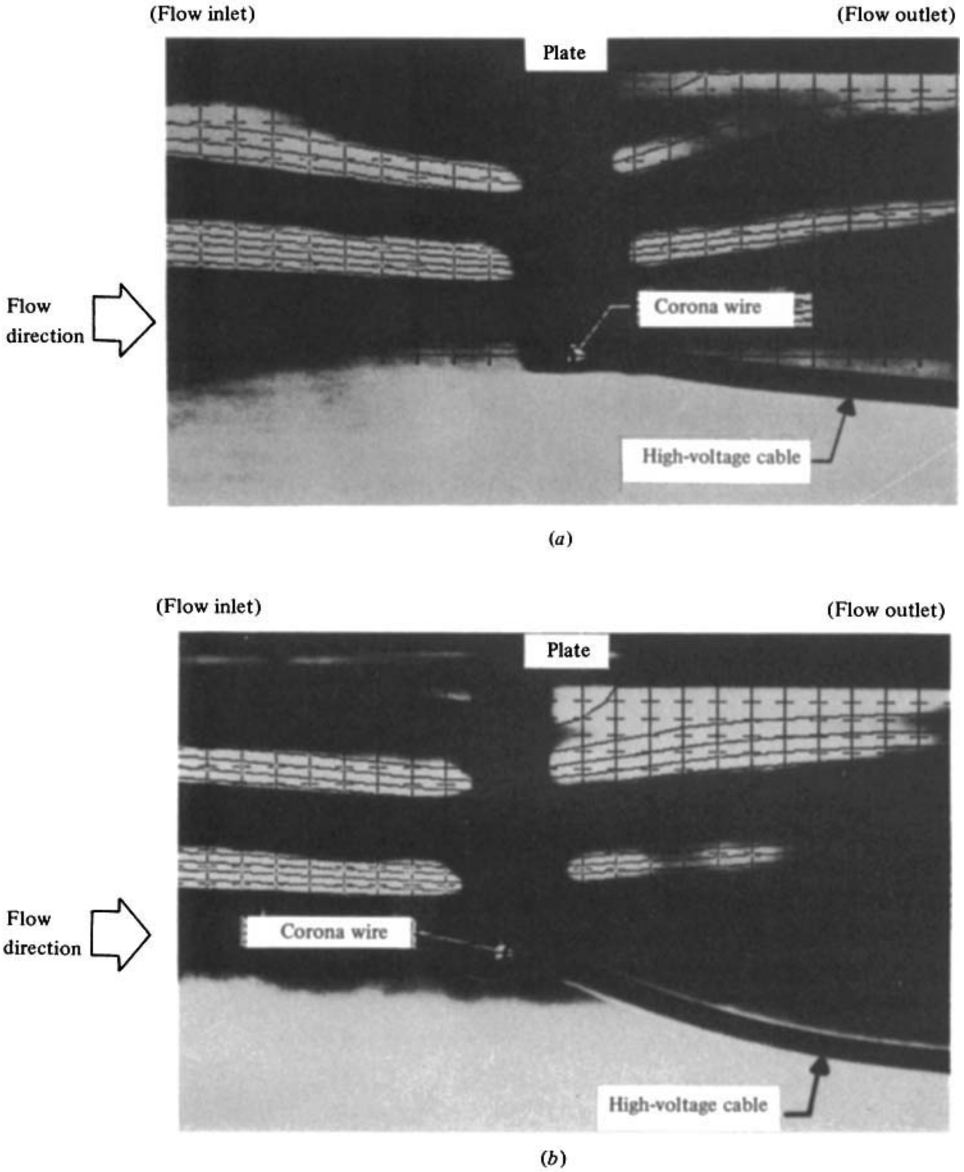

FIGURE 14. Direct overlay between experimental and numerical streamlines. White lines, experimental streamlines; solid lines, numerical streamlines; (*a*) $U_0 = 0{\cdot}91\ \mathrm{m\,s^{-1}}$, $R = 3600$, $E_0 = 5{\cdot}0\ \mathrm{kV\,cm^{-1}}$, $N_{EHD} = 1{\cdot}98$; (*b*) $U_0 = 1{\cdot}22\ \mathrm{m\,s^{-1}}$, $R = 4800$, $E_0 = 5{\cdot}0\ \mathrm{kV\,cm^{-1}}$, $N_{EHD} = 1{\cdot}49$.

the corona wire while the other cell, which is clockwise downstream of the channel, becomes diminishingly small. At $R = 2400$, figure 11 (*d*), all circulatory cells disappear, except one which is shifted toward the plate and becomes very small. This indicates that the flow interaction zone is reduced as R increases. The fluid entering the channel is gradually accelerated and deflected toward the centre-line of the channel due to the circulatory motion. At $R = 2400$, maximum velocity of the flow in the vicinity of the

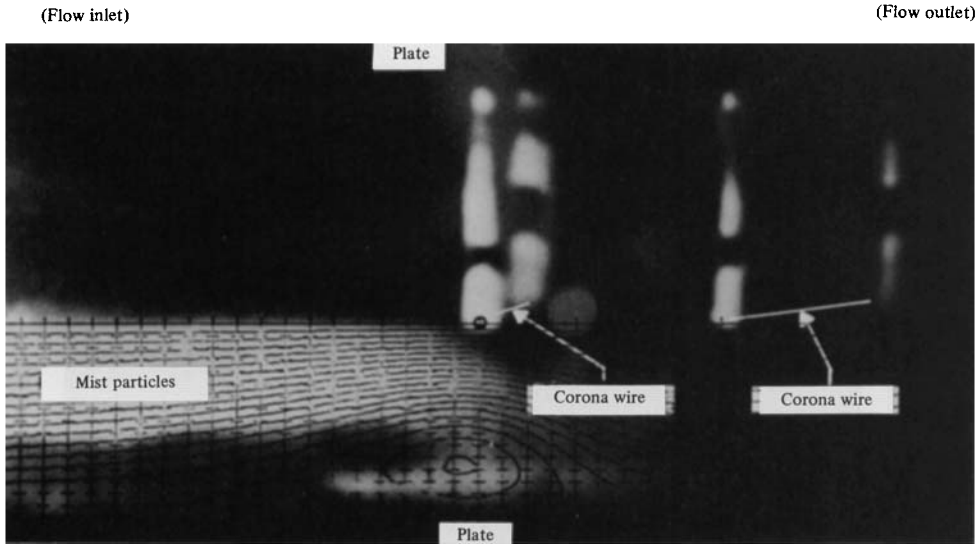

FIGURE 15. Direct overlay between the mist particle trajectory and the EHD streamlines. $U_0 = 0{\cdot}61$ m s^{-1}, $R = 2400$, $E_0 = 6{\cdot}0$ kV cm^{-1}.

wire reaches 2·08 times the inlet velocity. After passing the corona wire, the stream moves toward the plate. The flow decelerates as the flow approaches the outlet. As the Reynolds number is further increased, figure 11(*e*), the circulatory cell is decreased but remains above the corona wire which corresponds to the shift of the pressure peak. The flow near the plate and above the wire is significantly reduced, resulting in a reduction of shear stress. The circulatory cell becomes insignificant above the Reynolds number of 7200.

Two-wire configuration

Figures 12(*a*)–(*c*) show the flow interaction for the two-wire configuration. The computed streamline distribution is shown in figure 13(*a*)–(*b*). It should be noted that the vertical scale shown in figure 13(*a*)–(*b*) is twice as large as the horizontal scale. Figure 13(*a*) shows the secondary flow having two pairs of circulatory cells which corroborates Robinson's (1976) hypothesis.

As can be seen from the experimental and numerical results, all the clockwise cells disappear and only counterclockwise cells remain with increasing Reynolds number. A fluid particle entering the channel gradually moves toward the first wire. It is pushed back toward the plate and then is deflected toward the second wire at about the midpoint between the wires. After passing the second wire, the fluid particle is pushed toward the plate. A zigzag motion with accelerating and decelerating flow regions results. A large portion of the flow cross-section is blocked off by these induced circulatory cells.

The effects of the inlet and outlet boundary conditions and the number of mesh points on the numerical flow computations have also been considered. One way to evaluate the effect of the boundary condition is to change the length of the domain of the flow channel and see how the flow distribution in the domain of interest is affected. Two expanded flow regions were tried. The results were found to be in good agreement with the preceding cases, except in the vicinity of the inlet and exit boundaries. Two different grid sizes were also tried, namely 113×17 and 225×33, and indicated satisfactory agreement.

A direct overlay of the schlieren photographs on the computed streamlines demonstrates an excellent agreement with experimental measurement. This comparison is shown in figure 14(*a*)–(*b*).

(*c*) *Mist collection process in the EHD field*

Figure 15 illustrates the motion of mist particles as obtained with injection of the mineral oil smoke (mist). The calculated streamlines are superimposed. It can be seen that the paths of the mist particles follow very closely the calculated EHD path. This close correlation implies that the EHD actions are potentially important to particle collection processes and especially for submicron particles in which the migration velocity is small. This result suggests that the secondary flow is not strongly influenced by the charged particles since both gas and particle trajectories are similar.

5. Discussion

The effect of EHD on electrostatic precipitator performance appears to be significant. Observation of the flow interaction on the particles due to the secondary flow indicates that the secondary flow tends to reduce the transport of the dust particles towards the plate upstream of the corona wire and to enhance that downstream of the corona wire. It is also observed from figure 15 that the uniform particle concentrations, as assumed by Deutsch's analysis, is not sufficient.

The collection of dust particles onto the plate can also be influenced by EHD actions. Particles introduced near the centre-line of the channel, except when very close to the corona wire, may be more difficult to collect on the plate because both the coulomb and EHD forces are small. Because of this, dust may build up on the wire. Additionally, particles entering the precipitation zones near the plate may be precipitated only when the electrostatic force exceeds the EHD force on the particle.

It can also be deduced from a study of the figures that the shear stress along the wall is altered significantly by the presence of the EHD actions as compared to the non-EHD case. At low Reynolds numbers, for a given applied voltage (i.e. $R < 1800$ and $N_{\mathrm{EHD}} > 4{\cdot}0$), regions of greatly reduced shear stress occur generally ahead of the wire, and regions of significantly higher shear stress occur aft of the wire. Any such significant increase in surface shear stress can result in increased dust re-entrainment from the dust layer. At higher Reynolds numbers (i.e. $R > 3600$ and $N_{\mathrm{EHD}} < 2{\cdot}0$) the shear stress is reduced from that of the non-EHD case along the entire surface under the corona wire.

6. Conclusions

Experimental and theoretical studies on the secondary flow interaction in an electrostatic precipitator were performed with the focus on the one-wire and two-wire configurations. The theoretical model was found to be consistent with the experimental results. Although all the flow calculations were made for a fixed set of parameters, except the cross-flow velocity, the results can be extended to other sets of parameters having the same N_{EHD}. When N_{EHD} is above $0{\cdot}6$, the secondary flow interaction becomes significant and, when N_{EHD} is above 1·2, the effect of the secondary flow is extensive, due to the circulatory cell which is formed. Presentation of the computed streamlines was found to be quite useful in helping to explain the effect of the secondary flow on the precipitator performance. In determining the performance of an electrostatic precipitator, this work indicates that the actual dust particle velocity must not only be the sum of the effect of the electrostatic forces and the main-stream velocity, but also include the secondary flow caused by the electric wind. The Deutsch–Anderson efficiency equation, which is frequently used, does not include the EHD secondary flow. How to incorporate the secondary flow effect quantitatively into the precipitator efficiency equation is open for future studies.

REFERENCES

LEUTERT, G. & BOHLEN, B. 1972 The spatial trend of electric field strength and space charge density in plate-type electrostatic precipitators. *Staub-Reinhalt. Luft* **32**, 27–33 (in English).

NAKAMURA, S. 1977 *Computation Methods in Engineering and Science with Applications to Fluid Dynamics and Nuclear Systems.* Wiley-Interscience.

RAMADAN, D. E. & SOO, S. L. 1969 Electrohydrodynamic secondary flow. *Phys. Fluids* **12**, 1943–1945.

ROACHE, P. J. 1972 *Computation Fluid Dynamics.* Hermosa.

ROBINSON, M. 1976 Effects of the corona discharge on electric wind convection and eddy diffusion in an electrostatic precipitator. *ERDA, Health & Safety Lab. Rep.* HASL–301.

YABE, A., MORI, Y. & HIJIKATA, K. 1978 EHD study of the corona wind between wire and plate electrodes. *A.I.A.A.J.* **16**, 340–345.

YAMAMOTO, T. 1979 Electrohydrodynamic secondary flow interaction in an electrostatic precipitator. Ph.D. thesis, Ohio State University.

YAMAMOTO, Y., NAKAMURA, S. & VELKOFF, H. R. 1980 Numerical study of secondary flow interaction in an electrostatic precipitator. *Innovative Numerical Analysis for the Engineering Science*, pp. 3–12. University Press of Virginia.